Article

Computational design of transmembrane pores

https://doi.org/10.1038/s41586-020-2646-5

Received: 24 August 2019

Accepted: 29 May 2020

Published online: 26 August 2020

Check for updates

Chunfu Xu[1,2,3,12], Peilong Lu[1,2,4,5,12]✉, Tamer M. Gamal El-Din[6], Xue Y. Pei[7], Matthew C. Johnson[2], Atsuko Uyeda[8], Matthew J. Bick[1,2,10], Qi Xu[4,5], Daohua Jiang[6], Hua Bai[1,2], Gabriella Reggiano[1,2], Yang Hsia[1,2], TJ Brunette[1,2], Jiayi Dou[1,2,11], Dan Ma[4,5,9], Eric M. Lynch[2], Scott E. Boyken[1,2,10], Po-Ssu Huang[1,2,11], Lance Stewart[1], Frank DiMaio[1,2], Justin M. Kollman[2], Ben F. Luisi[7], Tomoaki Matsuura[8], William A. Catterall[6]✉ & David Baker[1,2,3]✉

Transmembrane channels and pores have key roles in fundamental biological processes[1] and in biotechnological applications such as DNA nanopore sequencing[2–4], resulting in considerable interest in the design of pore-containing proteins. Synthetic amphiphilic peptides have been found to form ion channels[5,6], and there have been recent advances in de novo membrane protein design[7,8] and in redesigning naturally occurring channel-containing proteins[9,10]. However, the de novo design of stable, well-defined transmembrane protein pores that are capable of conducting ions selectively or are large enough to enable the passage of small-molecule fluorophores remains an outstanding challenge[11,12]. Here we report the computational design of protein pores formed by two concentric rings of α-helices that are stable and monodisperse in both their water-soluble and their transmembrane forms. Crystal structures of the water-soluble forms of a 12-helical pore and a 16-helical pore closely match the computational design models. Patch-clamp electrophysiology experiments show that, when expressed in insect cells, the transmembrane form of the 12-helix pore enables the passage of ions across the membrane with high selectivity for potassium over sodium; ion passage is blocked by specific chemical modification at the pore entrance. When incorporated into liposomes using in vitro protein synthesis, the transmembrane form of the 16-helix pore—but not the 12-helix pore—enables the passage of biotinylated Alexa Fluor 488. A cryo-electron microscopy structure of the 16-helix transmembrane pore closely matches the design model. The ability to produce structurally and functionally well-defined transmembrane pores opens the door to the creation of designer channels and pores for a wide variety of applications.

Recent work on de novo membrane protein design has focused on compact bundles of helices without large central cavities[7,8]. De novo design of transmembrane proteins with large pores presents a more stringent thermodynamic challenge, because such proteins have a larger surface-area-to-volume ratio and therefore a lower density of stabilizing interactions. A homo-oligomeric architecture in which a cyclic arrangement of several identical copies of a single subunit surrounds the pore—as found in many natural protein pores—is attractive for protein design, because the subunit need not be a large protein. Soluble single-ring coiled-coil assemblies of peptide helices that surround central pores have been designed[13], but the transformation of soluble oligomeric protein pores into their membrane counterparts is challenging because of the altered thermodynamics of folding in the membrane and because of the possibility of undesired interactions between the non-polar residues introduced to interact with lipids and the residues at intersubunit interfaces. For example, the oligomerization state of coiled-coil assemblies has been shown to be very sensitive to the placement of non-polar residues[14], and so non-polar residues incorporated to interact with the bilayer could substantially alter the oligomeric state.

We set out to design transmembrane protein pores using a two-step approach. We reasoned that protein pores formed from two concentric rings of α-helices containing buried hydrogen-bond networks for structural specificity could be stable both in the water-soluble form and, after resurfacing the lipid-exposed residues with membrane-compatible hydrophobic residues, in the transmembrane form. The increased

[1]Institute for Protein Design, University of Washington, Seattle, WA, USA. [2]Department of Biochemistry, University of Washington, Seattle, WA, USA. [3]Howard Hughes Medical Institute, University of Washington, Seattle, WA, USA. [4]Zhejiang Provincial Laboratory of Life Sciences and Biomedicine, Key Laboratory of Structural Biology of Zhejiang Province, School of Life Sciences, Westlake University, Hangzhou, China. [5]Institute of Biology, Westlake Institute for Advanced Study, Hangzhou, China. [6]Department of Pharmacology, University of Washington, Seattle, WA, USA. [7]Department of Biochemistry, University of Cambridge, Cambridge, UK. [8]Department of Biotechnology, Graduate School of Engineering, Osaka University, Suita, Japan. [9]Department of Biological Structure, University of Washington, Seattle, WA, USA. [10]Present address: Lyell Immunopharma, Inc., Seattle, WA, USA. [11]Present address: Department of Bioengineering, Stanford University, Stanford, CA, USA. [12]These authors contributed equally: Chunfu Xu, Peilong Lu. ✉e-mail: lupeilong@westlake.edu.cn; wcatt@uw.edu; dabaker@uw.edu

interhelical interaction surfaces in such two-ring bundles could result in greater stability compared with single-ring structures—particularly for larger pore sizes—and, together with buried hydrogen-bond networks, provide greater structural robustness to conversion from soluble to transmembrane forms. We chose to focus on the design of homo-oligomeric cylindrical two-ring bundles consisting of a minimum of 12 closely packed helices—as parametrically designed two-ring bundles of ten or fewer helices generally do not contain pores large enough for solutes to traverse—using subunits containing between 2 and 4 helices to avoid having to build such large structures from a single polypeptide.

Designing an ion channel

We first explored the design of water-soluble pore containing helical bundles with a two-ring, six-fold symmetric topology, formed from monomeric subunits composed of an inner and an outer helix that are bridged with a short loop. Backbones were generated by sampling α-helical and superhelical parameters using a generalization of the Crick coiled-coil parameterization[15–17] (see Supplementary Information). After backbone generation and loop closure, we searched for hydrogen-bond networks across the intermolecular interfaces using Rosetta HBNet[18] and carried out combinatorial sequence optimization for the remaining residue positions, keeping the polar networks found by HBNet fixed. The interfacial core residues and backbone parameters of the inner helices were set to those of a previously characterized 'single-ring' helical bundle[13] to reduce the design space. Rosetta 'fold-and-dock'[19] structure prediction calculations were used to investigate the extent to which the designed sequences encode the design target topologies. Designs for which the lowest-energy sampled structures were close to the target design structures (Extended Data Fig. 1a) were selected for experimental characterization.

We obtained synthetic genes encoding the selected designs and expressed them in *Escherichia coli*. All three hexameric designs selected for experimental validation were well expressed and soluble in *E. coli*, and could be efficiently purified using nickel-affinity chromatography and size-exclusion chromatography (SEC). Multiangle light scattering (MALS, Extended Data Fig. 2a) and analytical ultracentrifugation (AUC, Extended Data Fig. 1c) indicated that one of the designs formed a single homogeneous species with the target oligomeric state. The circular dichroism spectrum of this hexameric design (denoted WSHC6, for water-soluble hairpin C6) showed that the structure was highly helical and stable to thermal denaturation up to 95 °C (Extended Data Fig. 1b). The small-angle X-ray scattering (SAXS) profile of WSHC6 was close to that computed from the design model, suggesting that WSHC6 folds into the desired shape in solution (Extended Data Fig. 1d). We determined the crystal structure of WSHC6 and found it to closely match the computational design model (Fig. 1a) with a Cα root-mean-square deviation (r.m.s.d.) of 0.89 Å. A chain of discrete water molecules occupies the WSHC6 channel (Fig. 1b, Extended Data Fig. 1e, Extended Data Table 1); the narrowest constriction is at Leu51 with a diameter of approximately 4 Å, as calculated by HOLE[20].

We next sought to convert the stable and structurally well-defined WSHC6 pore into a transmembrane hexameric pore (denoted TMHC6, for transmembrane hairpin C6). We redesigned the lipid-exposed residues (see Supplementary Information) and incorporated one ring of six glutamate residues (E-ring) and two rings of lysine residues (K-rings) at the openings of the central channel on the extracellular and intracellular side, respectively, to increase the polarity of the pore entrance and exit (Fig. 1c, Extended Data Fig. 3a, b). Similar rings are observed in the calcium channel Orai[21,22]. The narrowest regions of the TMHC6 pore in the design model are the E-ring (3.3 Å), the K-rings (4.3 Å and 5.7 Å) and two intervening rings of hydrophobic leucine residues (L-rings, 3.6 Å and 4.3 Å) (Fig. 1c). A synthetic gene was obtained for TMHC6 and the protein was expressed in *E. coli*, extracted from the membrane fraction with detergent, and purified by affinity chromatography and SEC (Extended Data Fig. 2c). TMHC6 eluted as a single peak during SEC, and circular dichroism measurements showed that the structure is α-helical and has a high thermal stability, with a circular dichroism spectrum at 95 °C similar to that at 25 °C (Fig. 1d). The protein sedimented as a hexamer in detergent solution in AUC experiments, consistent with the design model (Fig. 1e). Electron microscopy of negatively stained samples showed populations of particles that had shapes and sizes consistent with the design model (Extended Data Fig. 3c).

To investigate ion conductance by TMHC6, we performed whole-cell patch-clamp experiments on *Trichoplusia ni* insect cells (Hi5) expressing the designed transmembrane proteins. Using extracellular (bath) and intracellular (electrode) solutions containing 100 mM NaCl and 100 mM NaF, respectively, the TMHC6 construct exhibited a symmetric current–voltage relationship for inward and outward sodium-ion (Na^+) current as a function of membrane potential (Fig. 1f). Gadolinium ions (Gd^{3+})—a potent blocker of cation channels—blocked TMHC6 from the extracellular side, reducing the ion conductance to nearly the control value for untransfected cells (Fig. 1f). To test the ion selectivity, Hi5 cells expressing TMHC6 were bathed in a solution containing 100 mM of the chloride salt of the monovalent cations of potassium (K^+), Na^+ and caesium (Cs^+), and the methylammonium ion ($CH_3NH_3^+$). The patch pipettes contained the equivalent concentration of the fluoride salt of the same cation, except for $CH_3NH_3^+$, for which the pipette contained 100 mM caesium fluoride (CsF). TMHC6 showed a significantly higher conductance for K^+, with a current density of 600 pA pF^{-1} at +100 mV. The selectivity order was K^+ (600 pA pF^{-1}) ≫ $CH_3NH_3^+ = Cs^+$ (170 pA pF^{-1}) > Na^+ (60 pA pF^{-1}) ≈ Ba^{2+} (54 pA pF^{-1}) (Fig. 1g). By comparison, a previously designed transmembrane protein (TMHC2) without a pore[8] yielded a current density for K^+ of around 40 pA pF^{-1} at +100 mV, which was close to the background value (Extended Data Fig. 3d).

In the design model, the extracellular ring of six Glu44 residues is the site of cation entry (Fig. 2a). We tested this hypothesis by site-directed mutagenesis and chemical modification. Mutation of Glu44 to phenylalanine (E44F) removed the negative charge at the extracellular entry to the pore and reduced the conductance to 308 ± 81 pA pF^{-1} (mean ± s.e.m.), 51.3% of the control value (Extended Data Fig. 3d). This reduction probably results from a direct effect on ion traversal through the pore: TMHC6(E44F) is expressed at a similar level to the TMHC6 parent (Extended Data Fig. 3f), and the purified mutant protein has a similar solution behaviour to that of TMHC6 (Extended Data Fig. 2c). To further test the importance of this site, we constructed the E44H mutant in which Glu44 is mutated to histidine—removing the negative charge in this position and adding a partial positive charge. The divalent cation Cd^{2+} blocks the conductance of TMHC6, and threefold higher Cd^{2+} concentrations were required to block TMHC6(E44H), probably because of the reduced electrostatic attraction and/or disrupted metal coordination in the mutant protein (Fig. 2b). To enable a chemical modification approach, we constructed the E44C mutant in which Glu44 is mutated to cysteine; this removed the negative charge at the extracellular entry to the pore and reduced the conductance to 360 ± 36 pA pF^{-1}, 60% of the control. We then took advantage of the chemical reactivity of the substituted cysteine residue to test sulfhydryl reagents as pore blockers. We found that perfusion of three different methanethiosulfonates—the negatively charged MTSES, the positively charged MTSET and the hydrophobic MTS-TBAE—all completely blocked the ion conductance of TMHC6(E44C) within a few minutes under voltage-clamp control (Fig. 2c, d). The lack of dependence on charge or hydrophilicity suggests that these compounds function by direct steric blocking of the pore. The blockage by these reagents is entirely dependent on the introduced cysteine residue: they had no effect on the original TMHC6 design that lacks the cysteine (Fig. 2c, d). To determine whether covalent modification had any global effect on the folding or assembly of the pore, we expressed and purified TMHC6(E44C) from *E. coli* and incubated it with MTSES. Covalent modification was observed by mass

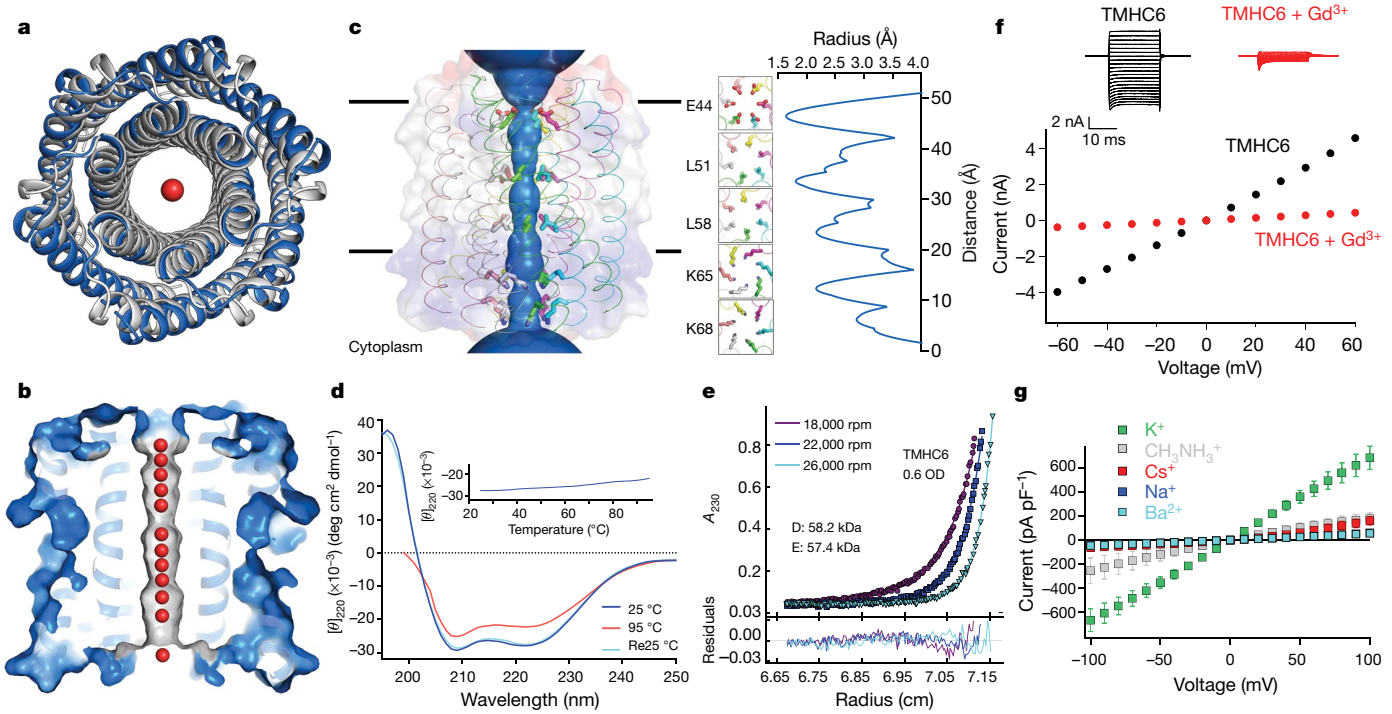

Fig. 1 | The X-ray crystal structure of the water-soluble hexameric WSHC6 and the ion conductivity of the 12-helix TMHC6 transmembrane channel. **a**, Superposition of the backbones of the crystal structure (blue) and the design model (grey) of WSHC6. The Cα r.m.s.d. between the crystal structure and the design model is 0.89 Å. The red sphere represents a water molecule. **b**, The cross-section of the WSHC6 channel. A chain of water molecules (red spheres) occupies the central pore (Extended Data Fig. 1e). **c**, Model of the TMHC6 channel. The permeation path, calculated by HOLE[20], is illustrated by the blue surface in the left panel. Constriction sites along the channel are the E-ring (E44), the K-rings (K65, K68), and two intervening L-rings (L51, L58). Right, the radius of the pore along the permeation path. **d**, Circular dichroism spectra and temperature melt curve (inset) of the TMHC6 channel. No apparent unfolding transition is observed up to 95 °C. The spectrum labelled Re25 °C was taken when the sample had cooled back to 25 °C after the thermal melt scan. $[\theta]_{220}$, molar ellipticity at 220 nm. **e**, AUC sedimentation–equilibrium curves at three different rotor speeds for TMHC6 yield a measured molecular mass of approximately 58 kDa, consistent with the designed hexamer. D and E indicate the molecular mass of the oligomer design and the molecular mass calculated from the experiment, respectively. A_{230}, absorbance (in arbitrary units (AU)) at 230 nm; OD, optical density. **f**, Conductivity in whole-cell patch-clamp experiment on insect cells expressing TMHC6. The channel blocker Gd^{3+} diminished ion conductance to a level equivalent to that of untransfected cells. **g**, TMHC6 has considerably higher conductance for K^+ than for Na^+, Cs^+, $CH_3NH_3^+$ and Ba^{2+}. Ten cells were measured for each permeant ion species; data are mean ± s.e.m.

spectrometry analysis (Extended Data Fig. 3e), but there was no change in pore assembly or solution behaviour more generally (Extended Data Fig. 2d), further suggesting that chemical modification blocks ion conductance by direct steric occlusion.

Taken together, the high ion selectivity, specific inhibition by multivalent cations, and complete block by MTS reagents acting at the extracellular entry to the pore strongly suggest that ion passage occurs through the designed central transmembrane pore. Leak conductances would not be expected to have these properties. As is the case for some naturally occurring channels, such as the physiologically important store-operated calcium channel Orai[23], single-channel recordings on TMHC6 did not yield clear signals. The single-channel conductance may be too low to measure reliably, perhaps because of the narrow diameter of the central non-polar lined portion of the pore.

The residue composition and structure of the conductive channel of TMHC6 are reminiscent of calcium-selective Orai channels, but TMHC6 is selective for K^+. This selectivity probably reflects the narrow 3.3 Å constriction of the TMHC6 pore, which only allows conductance of at least partially dehydrated K^+. Natural potassium channels have selectivity filters of similar size and conduct K^+ through direct interactions with backbone carbonyls, without any intervening equatorial waters of hydration[24]. By contrast, voltage-gated sodium and calcium channels—which conduct hydrated Na^+ and Ca^{2+} (refs. [25,26])—have selectivity filters that are 4.6 $Å^2$, well suited to accommodate hydrated sodium and calcium ions[25–27] but not hydrated potassium ions. The ability to design transmembrane pores de novo lays the foundation for broad exploration of the pore diameters and chemical interactions that are required for selective conductance of a wide range of ions. This understanding should enable the design of channels that directly modulate cell function. As a first step in this direction, we expressed TMHC6 in a yeast strain that requires potassium for growth, and found that the growth rate increased considerably in a K^+-dependent manner (Extended Data Fig. 4).

Building a larger transmembrane nanopore

To explore the generation of larger transmembrane pores that are capable of transporting organic molecules larger than single ions, we designed water-soluble helical bundles with eight-fold symmetry. Our approach was similar to that described above for WSHC6 except that a starting 'single-ring' template was not used; instead, the structure and sequence of the inner ring of helices were sampled de novo in parallel to those of the outer ring. We obtained synthetic genes encoding selected octameric pore designs and expressed them in *E. coli*. Four out of five of the octameric designs were well expressed and soluble in *E. coli*, and could be purified by nickel-affinity chromatography and SEC. However, none of the designs populated only the target octameric state. There are only small differences in interface geometry between C7, C8 and C9 assemblies (the angles between subunits are 51°, 45° and 40°, respectively), and mixtures were observed for most of the

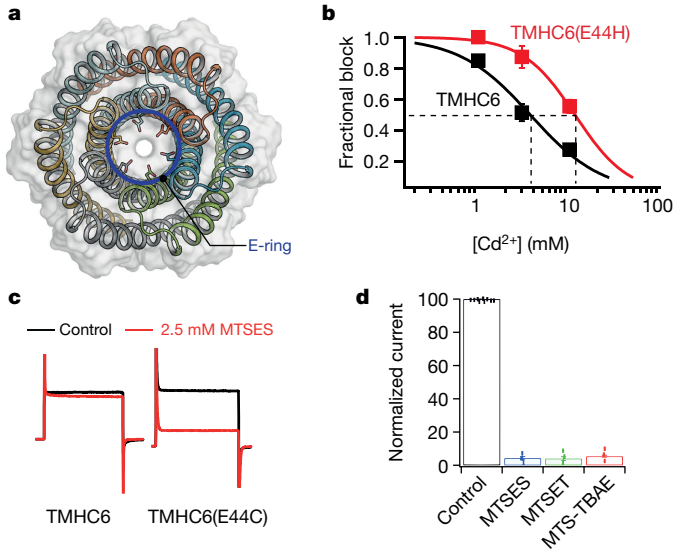

Fig. 2 | Blocking of the ion conductance of TMHC6 by chemical modification at the pore entrance. a, The extracellular ring of six Glu44 residues (E-ring, shown as sticks) is a likely site for cation entry. **b**, Blocking of the K^+ conductance of TMHC6 and the E44H mutant by Cd^{2+}. Threefold higher Cd^{2+} concentrations were required to block TMHC6(E44H) compared with TMHC6, probably because of the reduced electrostatic attraction in the former. Three cells were measured for each concentration; data are mean ± s.e.m. **c**, **d**, Blocking of the conductance of TMHC6(E44C) using cysteine reactive reagents. In **c**, the *y* axis shows the current amplitude and the *x* axis indicates the time scale. Negatively charged MTSES, positively charged MTSET, and hydrophobic MTS-TBAE all completely blocked the ion conductance of TMHC6(E44C) within a few minutes under voltage-clamp control, whereas they had no effect on TMHC6 in control experiments. Nine cells for the control and three cells for each reagent were measured. In **d**, the bars represent the mean of the measurements and individual data points are shown.

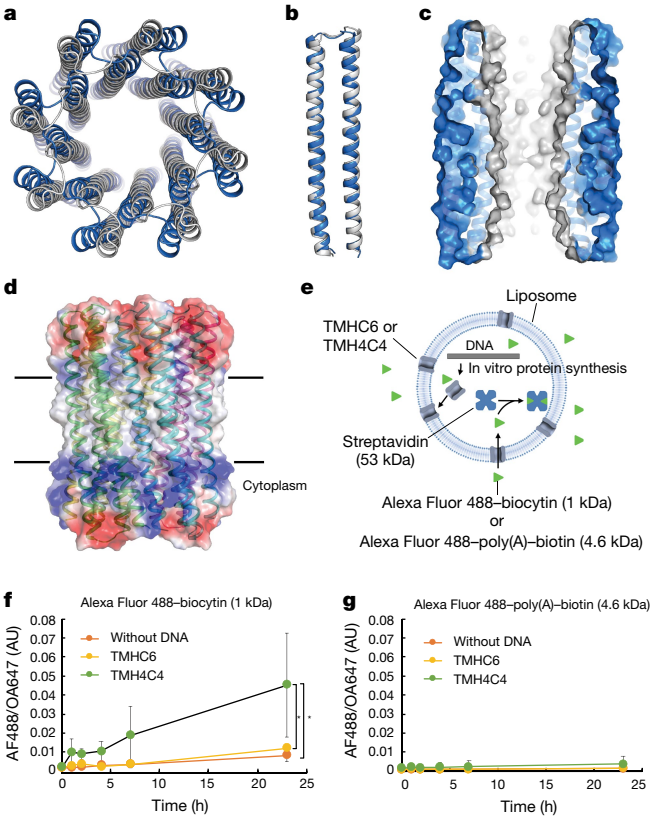

Fig. 3 | The X-ray crystal structure of water-soluble WSHC8 and the characterization of the 16-helix TMH4C4 transmembrane channel. **a**, **b**, Superposition of the full octameric assemblies and the monomeric subunits of the crystal structure (blue) and the design model (grey) of WSHC8. The Cα r.m.s.d. is 2.51 Å (octamer) and 0.97 Å (monomers). The larger deviation for the octamer is caused by the slight tilting of the hairpin monomers along the superhelical axis of the complex. **c**, The cross-section of the WSHC8 channel. **d**, Model of TMH4C4 with 16 transmembrane helices. The electrostatic surface of the neutral transmembrane regions is shown in grey. **e**, Liposome permeability assay. Membrane channels are generated by in vitro translation inside streptavidin-containing liposomes, biotin-labelled fluorescent dyes are added to the surrounding buffer, and the amount of dye trapped inside the liposomes is measured by flow cytometry. **f**, **g**, TMH4C4 functions as a size-dependent transmembrane sieve. Incorporation of TMH4C4 into liposomes enabled the accumulation of the 1 kDa but not the 4.6 kDa fluorescent dye, whereas TMHC6 disallowed both. Shown are the time courses of the median values of the histogram of Alexa Fluor 488/Ovalbumin conjugated to Alexa Fluor 647 (AF488/OA647) fluorescence (Extended Data Fig. 6e), which represents the concentration of the Alexa Fluor 488 inside the liposome. $n = 7$; data are mean (of the obtained median values) ± s.e.m. *$P = 0.0128$ (TMH4C4 vs control) and 0.0220 (TMH4C4 vs TMHC6); two-sided Student's paired *t*-test. In control experiments performed with α-haemolysin from *Staphylococcus aureus*, a well-studied channel-forming protein[33] with a pore constriction of approximately 15 Å, only the smaller dye accumulated (Extended Data Fig. 6f, g), suggesting that—as intended—the assay measures solute passage through the transmembrane pores.

designs. We reasoned that achieving a well-defined C8 state would require more precise interface definition; therefore, we carried out a second round of C8 designs with larger intersubunit interaction surface areas (Extended Data Fig. 5a, b) and more hydrogen-bond networks across the interface. Ten out of fifteen of the second-round designs that passed the in silico test (Extended Data Fig. 1f) were expressed and soluble in *E. coli*, and two were found to be monodisperse and octameric by MALS analysis (Extended Data Fig. 2b). One of the two was further confirmed by AUC (Extended Data Fig. 1h). The circular dichroism spectrum of the AUC-verified octameric design (denoted WSHC8, for water-soluble hairpin C8) showed that the structure was highly helical and had a melting temperature of 85 °C (Extended Data Fig. 1g). We again found excellent agreement between the experimental and calculated SAXS profiles, indicating that WSHC8 folds into the desired shape in solution (Extended Data Fig. 1i).

We determined the crystal structure of WSHC8 (Fig. 3a, b, Extended Data Table 1) and found that the Cα r.m.s.d. values between the crystal structure and the design model for the monomeric subunit and the full octameric pore were 0.97 Å and 2.51 Å, respectively. The larger deviation in this case compared with WSHC6 is caused by the slight tilting of the hairpin monomers along the superhelical axis of the complex (Extended Data Fig. 1j). As in the design model, the crystal structure contains a long and continuous central channel with an inner diameter of approximately 10 Å as calculated by HOLE. We converted WSHC8 into an octameric membrane-spanning pore (TMHC8) by redesigning the membrane-exposed and pore-facing residues of the crystal structure (see Supplementary Information, Extended Data Fig. 5c, d). The design model has a central pore with a diameter of 10 Å and a transmembrane span of 31 Å. A gene encoding TMHC8 was synthesized, the protein expressed in *E. coli*, and the membrane fraction purified and solubilized in detergent. After affinity chromatography, the protein eluted as a monodisperse peak during SEC (Extended Data Fig. 2e). Circular dichroism measurements showed that TMHC8 had the expected α-helical secondary structure with a melting temperature of 75 °C (Extended Data Fig. 5e). AUC experiments showed that TMHC8 formed complexes with a molecular mass of 98.9 kDa, which lies in between the masses of a 14-helix heptamer and a 16-helix octamer (Extended Data Fig. 5g). To resolve this ambiguity, we linked two monomers of TMHC8 together using a short loop to create a four-helix subunit. This redesign, denoted

TMH4C4 (Fig. 3d), was purified to homogeneity using nickel-affinity chromatography and SEC (Extended Data Fig. 2f). Circular dichroism spectroscopy showed that TMH4C4 was fully α-helical and was thermally stable up to 95 °C (Extended Data Fig. 5f). AUC experiments showed that TMH4C4 sedimented as a tetramer in detergent solution, consistent with the 16-helix design model (Extended Data Fig. 5h).

Expression of the designed larger transmembrane nanopore in insect cells resulted in cell death, probably because of induced cell permeability; we were therefore unable to assess the channel activity in these cells. Instead, we used a liposome-based assay coupled to in vitro protein synthesis[28–30]. TMHC6 and TMH4C4 were produced inside liposomes containing streptavidin, and biotinylated Alexa Fluor 488 (which has a molecular mass of around 1 kDa) was added outside (Fig. 3e). SEC analysis revealed that the in vitro-synthesized TMHC6 and TMH4C4 had similar elution volumes to the bacterially expressed and purified proteins (Extended Data Fig. 6a). Consistent with the much larger pore radius of TMH4C4 compared with TMHC6, we observed considerably more accumulation of dye within proteoliposomes containing only TMH4C4 than in proteoliposomes containing an equivalent amount of TMHC6, or in empty liposomes (Fig. 3f, Extended Data Fig. 6b, c, e). The narrowest dimension of the head group of the fluorophore is approximately 12 Å (Extended Data Fig. 6d), whereas the nominal diameter of the constriction region of the TMH4C4 pore is estimated to be 10 Å by HOLE; thermal fluctuations of the side chains and backbone probably allow for permeation by the fluorophore. By contrast, the 3.3 Å constriction of TMHC6 is far too narrow to allow the passage of fluorophores. Increasing the size of the fluorescent conjugate to 4.6 kDa—by inserting polyadenine oligo DNA (A11) between Alexa Fluor 488 and biotin—blocked passage through both the TMHC6 and the TMH4C4 pores (Fig. 3g), consistent with the estimated hydrodynamic diameter of this compound of 30 Å[31].

In seeking to obtain an overall structure of the 16-helix transmembrane channel, we used cryogenic electron microscopy (cryo-EM) to determine the three-dimensional (3D) structure of TMH4C4. The protein was concentrated to around 6 mg ml^{-1}, applied to EM grids, and cryo-EM images were collected and processed following standard protocols (Extended Data Fig. 7a–e). To avoid potential bias, C1 symmetry was applied for automatic image processing and classification; this yielded a dominant 16-helix form containing about 40% of all the 3D classified particles with the most continuous and intact map among all classes. Further classification and refinement focused on this set of particles resulted in a 5.9 Å resolution map from 64,739 (out of a total of 1,559,110 for 3D classification) selected particles (Fig. 4a, Extended Data Fig. 7d, e, Extended Data Table 2). The cryo-EM structure clearly shows the formation of a 16-helix assembly with a large central pore, consistent with the design model built from the crystal structure of the soluble form (Fig. 4a). Density encircling the membrane-spanning region probably originates from surrounding detergent molecules (Extended Data Fig. 7e, f). A structure model of TMH4C4 built on the basis of the EM map (Fig. 4a, b) showed some deviation among the four protomers, so the tetramer is not perfectly symmetric (Fig. 4c); however, the central-pore-containing 16-helix structure corresponding to the original TMH4C4 design is clearly resolved, and aligns well with the design model (Fig. 4b).

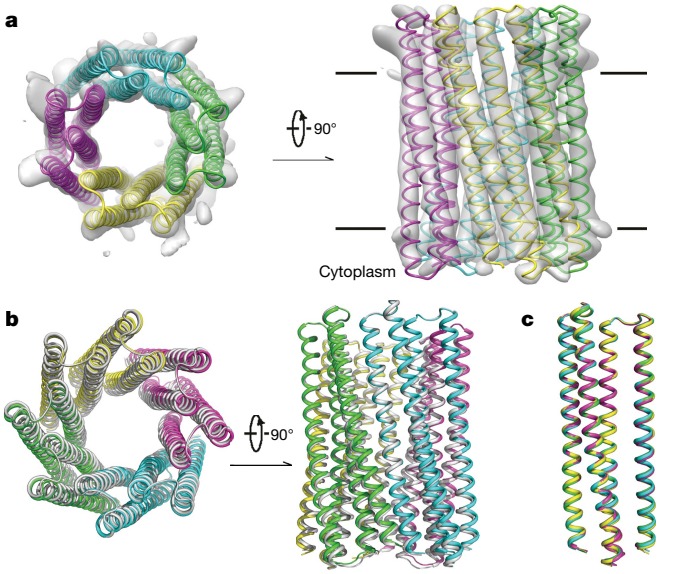

Fig. 4 | Cryo-EM structures of the 16-helix TMH4C4 transmembrane channel. a, Cryo-EM density (grey surface) and structure model (coloured ribbon) of the 16-helix TMH4C4 protein. Electron microscopy maps, generated in Chimera[34], are shown in two perpendicular views. **b**, Superposition of the cryo-EM structure (coloured) and design model based on the crystal structure of the soluble form (grey) of TMH4C4. **c**, Structure alignment of the four protomers in one tetrameric cryo-EM structure of TMH4C4.

Conclusion

Our advances in designing structurally well-defined transmembrane pores (for comparison to previous de novo membrane protein designs, see Extended Data Fig. 8), like advances in protein design generally[8,10,32], both inform our understanding of general principles of protein biophysics and open the door for a wide range of applications. From the perspective of membrane-protein folding, our success in designing transmembrane homo-oligomeric structures with subunit interfaces that contain hydrogen-bond networks suggests that the combination of the substantial buried surface area and polarity of the interaction surfaces makes these structures robust to changes in the surrounding environment and reduces confounding effects that result from interactions between the hydrophobic lipid-facing residues during folding. This approach enables the construction of substantial pores with environments very different from that of the surrounding lipids: the TMHC6 pore clearly shows selective transmembrane ion conductance, and the 10 Å-diameter TMH4C4 pore—clearly evident in the cryo-EM structure—is lined with polar residues and provides passage to solutes as large as biotinylated Alexa Fluor 488.

Our strategy—first designing soluble pore-containing structures and then converting the stable designs into transmembrane proteins after determination of the crystal structure—leverages the considerably more straightforward structural characterization of soluble proteins as a key step towards building complex transmembrane proteins with a high success rate (see Supplementary Information). Building on the channels described here, custom design now provides a platform through which to understand the underlying chemistry and physics of solute permeation and selectivity by modulating pore structures and selectivity filters in ways that are not possible with native channels, and also enables a wide range of applications. Among many possibilities, custom-designed pores could provide new routes to generating membranes with selective permeabilities, sensing molecules in the environment, and controlling cellular behaviour.

Online content

Any methods, additional references, Nature Research reporting summaries, source data, extended data, supplementary information, acknowledgements, peer review information; details of author contributions and competing interests; and statements of data and code availability are available at https://doi.org/10.1038/s41586-020-2646-5.

1. Gilbert, R. J. C., Bayley, H. & Anderluh, G. Membrane pores: from structure and assembly, to medicine and technology. *Phil. Trans. R. Soc. Lond. B* **372**, 20160208 (2017).
2. Eisenstein, M. An ace in the hole for DNA sequencing. *Nature* **550**, 285–288 (2017).

3. Kasianowicz, J. J., Brandin, E., Branton, D. & Deamer, D. W. Characterization of individual polynucleotide molecules using a membrane channel. *Proc. Natl Acad. Sci. USA* **93**, 13770–13773 (1996).
4. Clarke, J. et al. Continuous base identification for single-molecule nanopore DNA sequencing. *Nat. Nanotechnol.* **4**, 265–270 (2009).
5. Lear, J. D., Wasserman, Z. R. & DeGrado, W. F. Synthetic amphiphilic peptide models for protein ion channels. *Science* **240**, 1177–1181 (1988).
6. Akerfeldt, K. S., Lear, J. D., Wasserman, Z. R., Chung, L. A. & DeGrado, W. F. Synthetic peptides as models for ion channel proteins. *Acc. Chem. Res.* **26**, 191–197 (1993).
7. Joh, N. H. et al. De novo design of a transmembrane Zn^{2+}-transporting four-helix bundle. *Science* **346**, 1520–1524 (2014).
8. Lu, P. et al. Accurate computational design of multipass transmembrane proteins. *Science* **359**, 1042–1046 (2018).
9. Mahendran, K. R. et al. A monodisperse transmembrane α-helical peptide barrel. *Nat. Chem.* **9**, 411–419 (2017).
10. Mravic, M. et al. Packing of apolar side chains enables accurate design of highly stable membrane proteins. *Science* **363**, 1418–1423 (2019).
11. Joh, N. H., Grigoryan, G., Wu, Y. & DeGrado, W. F. Design of self-assembling transmembrane helical bundles to elucidate principles required for membrane protein folding and ion transport. *Phil. Trans. R. Soc. Lond. B* **372**, 20160214 (2017).
12. Niitsu, A., Heal, J. W., Fauland, K., Thomson, A. R. & Woolfson, D. N. Membrane-spanning α-helical barrels as tractable protein-design targets. *Phil. Trans. R. Soc. Lond. B* **372**, 20160213 (2017).
13. Thomson, A. R. et al. Computational design of water-soluble α-helical barrels. *Science* **346**, 485–488 (2014).
14. Rhys, G. G. et al. Maintaining and breaking symmetry in homomeric coiled-coil assemblies. *Nat. Commun.* **9**, 4132 (2018).
15. Crick, F. H. C. The Fourier transform of a coiled-coil. *Acta Crystallogr.* **6**, 685–689 (1953).
16. Grigoryan, G. & Degrado, W. F. Probing designability via a generalized model of helical bundle geometry. *J. Mol. Biol.* **405**, 1079–1100 (2011).
17. Huang, P. S. et al. High thermodynamic stability of parametrically designed helical bundles. *Science* **346**, 481–485 (2014).
18. Boyken, S. E. et al. De novo design of protein homo-oligomers with modular hydrogen-bond network-mediated specificity. *Science* **352**, 680–687 (2016).
19. Das, R. et al. Simultaneous prediction of protein folding and docking at high resolution. *Proc. Natl Acad. Sci. USA* **106**, 18978–18983 (2009).
20. Smart, O. S., Neduvelil, J. G., Wang, X., Wallace, B. A. & Sansom, M. S. P. HOLE: a program for the analysis of the pore dimensions of ion channel structural models. *J. Mol. Graph.* **14**, 354–360 (1996).
21. Hou, X., Pedi, L., Diver, M. M. & Long, S. B. Crystal structure of the calcium release-activated calcium channel Orai. *Science* **338**, 1308–1313 (2012).
22. Hou, X., Burstein, S. R. & Long, S. B. Structures reveal opening of the store-operated calcium channel Orai. *eLife* **7**, e36758 (2018).
23. Dynes, J. L., Amcheslavsky, A. & Cahalan, M. D. Genetically targeted single-channel optical recording reveals multiple Orai1 gating states and oscillations in calcium influx. *Proc. Natl Acad. Sci. USA* **113**, 440–445 (2016).
24. Jiang, Y. et al. X-ray structure of a voltage-dependent K^+ channel. *Nature* **423**, 33–41 (2003).
25. Payandeh, J., Scheuer, T., Zheng, N. & Catterall, W. A. The crystal structure of a voltage-gated sodium channel. *Nature* **475**, 353–358 (2011).
26. Tang, L. et al. Structural basis for Ca^{2+} selectivity of a voltage-gated calcium channel. *Nature* **505**, 56–61 (2014).
27. Pan, X. et al. Structure of the human voltage-gated sodium channel $Na_v1.4$ in complex with β1. *Science* **362**, eaau2486 (2018).
28. Fujii, S. et al. Liposome display for in vitro selection and evolution of membrane proteins. *Nat. Protoc.* **9**, 1578–1591 (2014).
29. Fujii, S., Matsuura, T., Sunami, T., Kazuta, Y. & Yomo, T. In vitro evolution of α-hemolysin using a liposome display. *Proc. Natl Acad. Sci. USA* **110**, 16796–16801 (2013).
30. Dwidar, M. et al. Programmable artificial cells using histamine-responsive synthetic riboswitch. *J. Am. Chem. Soc.* **141**, 11103–11114 (2019).
31. Sim, A. Y. L., Lipfert, J., Herschlag, D. & Doniach, S. Salt dependence of the radius of gyration and flexibility of single-stranded DNA in solution probed by small-angle X-ray scattering. *Phys. Rev. E* **86**, 021901 (2012).
32. Huang, P.-S., Boyken, S. E. & Baker, D. The coming of age of de novo protein design. *Nature* **537**, 320–327 (2016).
33. Song, L. et al. Structure of staphylococcal α-hemolysin, a heptameric transmembrane pore. *Science* **274**, 1859–1865 (1996).
34. Pettersen, E. F. et al. UCSF Chimera—a visualization system for exploratory research and analysis. *J. Comput. Chem.* **25**, 1605–1612 (2004).

Reporting summary

Further information on research design is available in the Nature Research Reporting Summary linked to this paper.

Data availability

Coordinates and structure files have been deposited to the Protein Data Bank with accession codes 6TJ1 (WSHC6, $P2_122_1$), 6TMS (WSHC6, P1) and 6O35 (WSHC8). An electron microscopy map of TMH4C4 and the associated structure model have been deposited in the Electron Microscopy Data Bank and Protein Data Bank with accession codes EMD-30126 and 6M6Z, respectively. Source data are provided with this paper.

Code availability

All program code is in Rosetta distribution (https://www.rosettacommons.org). Example design protocols are provided in the Supplementary Information.

Acknowledgements We thank A. Kang for assistance with crystallization; B. Sankaran of the Berkeley Center for Structural Biology at the Advanced Light Source for help with X-ray diffraction data collection; J. Sumida for AUC support; L. Carter for assistance with SEC–MALS; U. Nattermann, Q. Zhou and H. Shen for assistance with EM; SIBYLS mail-in SAXS program at the Advanced Light Source (ALS) for SAXS data collection; L. Jan, T. Cheng and R. Zhou from UCSF for sharing yeast strain SGY1528; and Rosetta@Home volunteers for contributing computing resources. The cryo-EM work was performed at the Cryo-EM Facility of Westlake University. We thank the Arnold and Mabel Beckman Cryo-EM Center at the University of Washington for access to electron microscopes, the Information Technology Center of Westlake University for providing computation support, and the Mass Spectrometry and Metabolomics Core Facility of Westlake University for mass spectrometry analysis. This work was supported by the Howard Hughes Medical Institute, the Air Force Office of Scientific Research (FA9550-18-1-0297) and NSF grant CHE 1629214. W.A.C. was supported by NIH research grant R35 NS111573. P.L. was supported by NSFC Project 31901054, Tencent Foundation and the foundation of Westlake University. SAXS data collection at SIBYLS is funded through DOE BER Integrated Diffraction Analysis Technologies (IDAT) program and NIGMS grant P30 GM124169-01, ALS-ENABLE. T.M. was in part supported by KAKENHI grants 17H00888 from JSPS. B.F.L. and X.Y.P. are supported by a Wellcome Trust Investigator award (200873/Z/16/Z). The ALS-ENABLE beamlines are supported in part by the National Institutes of Health, National Institute of General Medical Sciences, grant P30 GM124169-01 and the Howard Hughes Medical Institute. The Advanced Light Source is a Department of Energy Office of Science User Facility under contract number DE-AC02-05CH11231.

Author contributions C.X., P.L., T.M.G., L.S., T.M., W.A.C. and D.B. planned the research and designed experiments. C.X., P.L. and D.B. designed the proteins. C.X., P.L., T.M.G., J.D., T.M., W.A.C. and D.B. wrote the manuscript. C.X. and P.L. carried out biophysical characterizations. T.M.G. and W.A.C. performed patch–clamp experiments and analysed data. A.U. and T.M. performed liposome permeability assays and analysed data. X.Y.P., M.J.B. and B.F.L. solved crystal structures. P.L., Q.X., M.C.J. and J.M.K. determined the cryo-EM structure. G.R. and F.D. refined the cryo-EM structure. J.D. carried out the yeast growth assay. D.J. and D.M. prepared samples for patch–clamp experiments. E.M.L. took negatively stained electron micrographs. H.B., Y.H., T.B., S.E.B. and P.-S.H. helped with design calculations. All authors discussed the results and commented on the manuscript.

Competing interests The University of Washington has submitted a US provisional patent application (63/017,810) that covers the computational design of transmembrane pores described in this paper, listing C.X., P.L., T.M.G., W.A.C. and D.B. as inventors.

Additional information
Supplementary information is available for this paper at https://doi.org/10.1038/s41586-020-2646-5.
Correspondence and requests for materials should be addressed to P.L., W.A.C. or D.B.
Peer review information *Nature* thanks Eric Gouaux and the other, anonymous, reviewer(s) for their contribution to the peer review of this work.
Reprints and permissions information is available at http://www.nature.com/reprints.

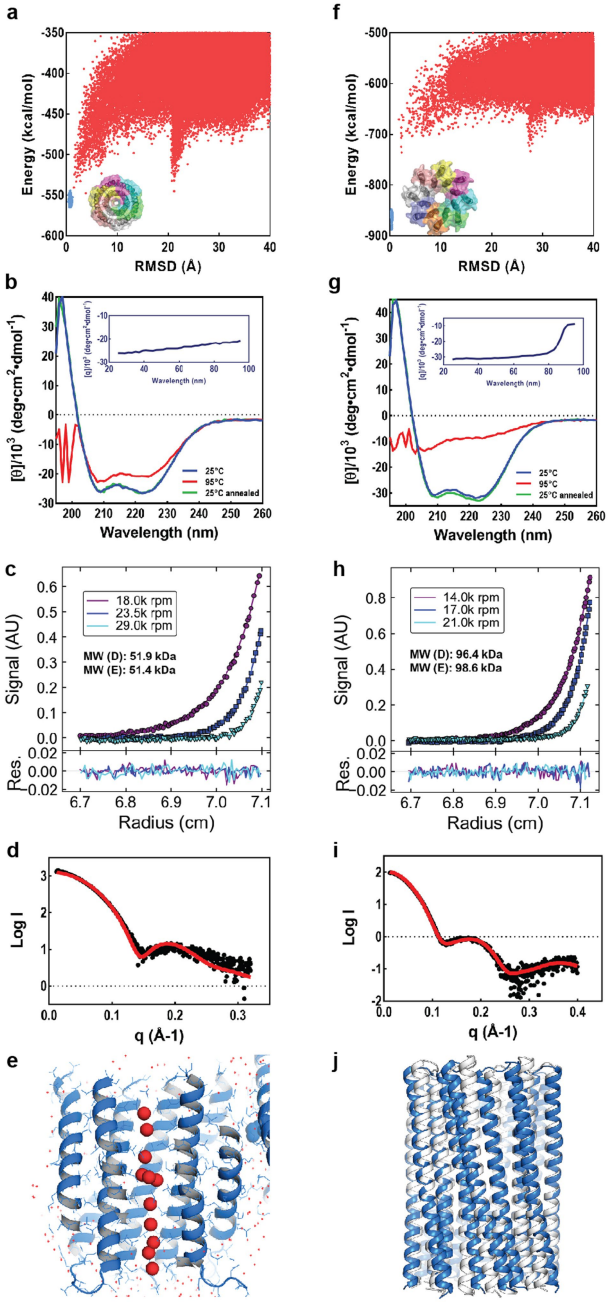

Extended Data Fig. 1 | Design and characterization of water-soluble pores. **a**, **f**, Design models (insets) and energy versus r.m.s.d. plots generated from Rosetta 'fold-and-dock' structure prediction calculations. The predicted structures converge on the design models with r.m.s.d. values less than 2.0 Å. Structures in the alternative energy minima at large r.m.s.d. positions also recapitulate the design models but with chain identities in the r.m.s.d. calculations reversed. **b**, **g**, Wavelength-scan and temperature-scan (insets) circular dichroism spectra. WSHC6 does not melt up to 95 °C, while WSHC8 has a melting temperature of 85 °C. The overlap of the pre- and post-annealing circular dichroism spectra indicates that the thermal denaturation is reversible. **c**, **h**, Representative analytical ultracentrifugation sedimentation-equilibrium curves at three different rotor speeds for WSHC6 and WSHC8, 0.2 OD_{230} and 0.3 OD_{230} in PBS (pH 7.4), respectively. The determined oligomeric states match those of the design models. **d**, **i**, Small-angle X-ray scattering (SAXS) characterization. The experimental scattering profiles (black) are similar to scattering profiles computed from the design models (red). **e**, The chain of water molecules in the pore of WSHC6 crystal structure (red spheres) is verified by processing the data and refining the structure in the P1 space group. **j**, Overlay of the crystal structure (blue) and the design model (grey) of WSHC8. Helices are more tilted in the crystal structure than in the design model.

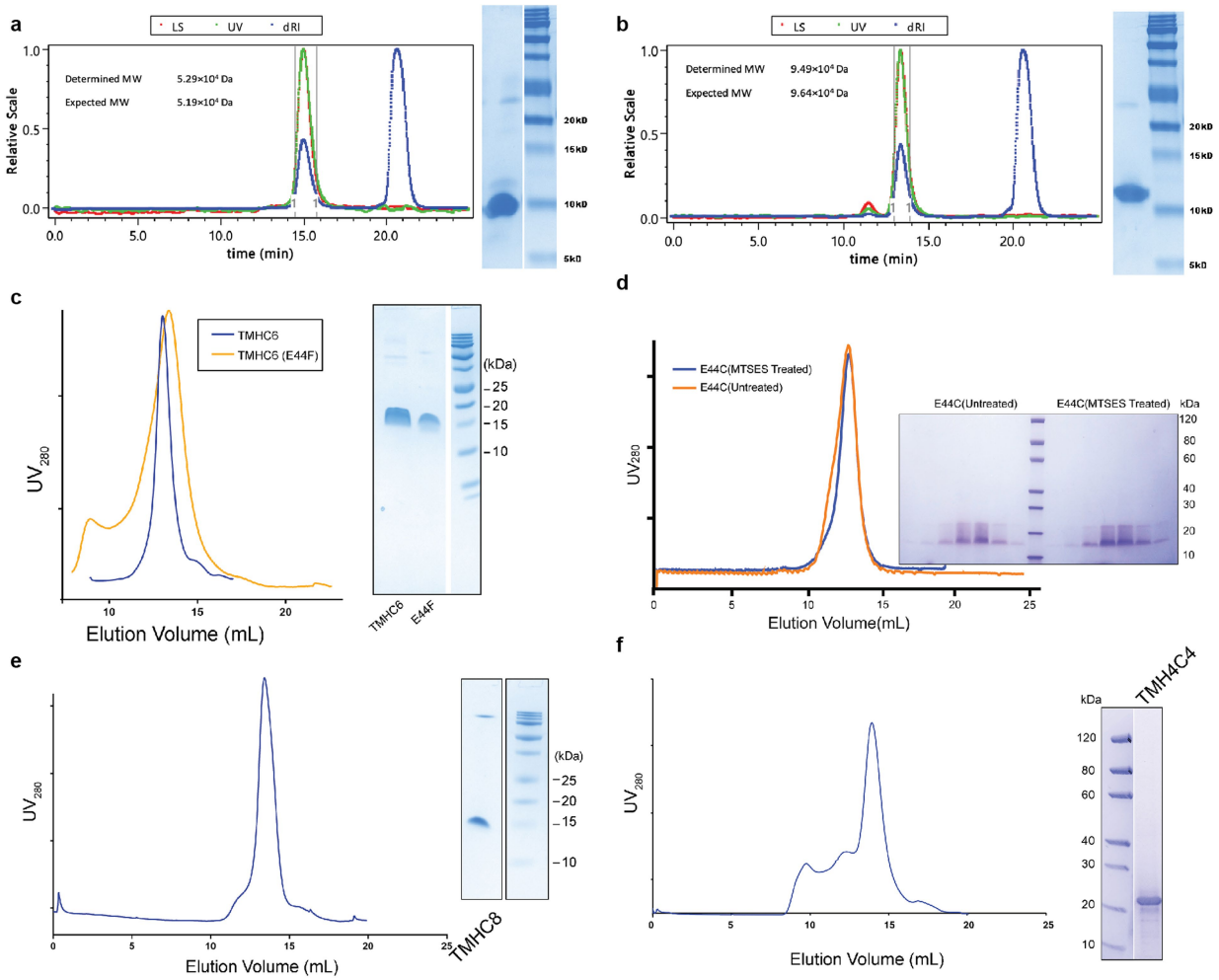

Extended Data Fig. 2 | Representative SEC and SDS–PAGE of the designed proteins. a, **b**, WSHC6 and WSHC8. Molecular masses are determined by coupling SEC with MALS. **c**, TMHC6 and the E44F mutant. **d**, TMHC6(E44C) treated or untreated with MTSES. **e**, TMHC8. **f**, TMH4C4. These experiments were repeated twice with similar results.

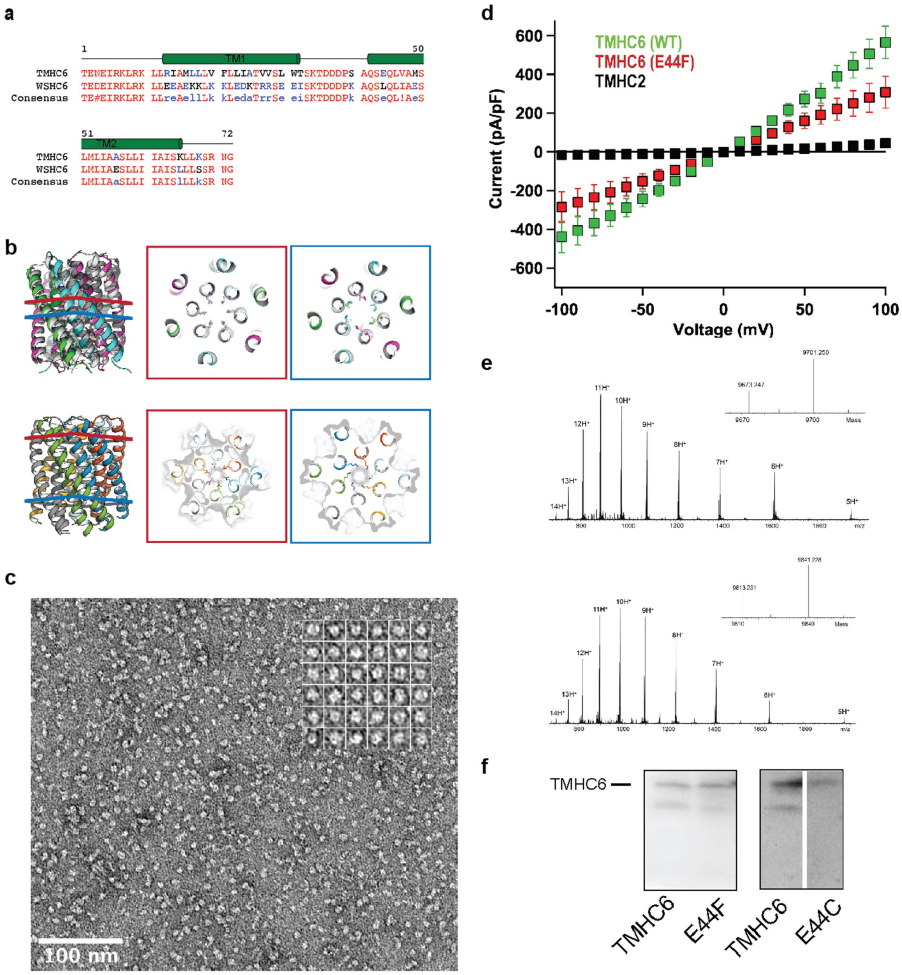

Extended Data Fig. 3 | Comparisons between WSHC6 and TMHC6 and additional characterizations of TMHC6 and mutants. a, Sequence alignment of TMHC6 with WSHC6. **b**, Pore-lining residues in WSHC6 and TMHC6. Top row, overlay of the crystal structure (colours) and the design model (grey) of WSHC6. The pore is lined with alternating leucine (red layer) and isoleucine (blue layer) residues. Bottom row, the TMHC6 pore is lined with E44 ring (red layer) and K65 ring (blue layer) at the extracellular and intracellular sides, respectively. **c**, Negative stain EM for TMHC6 in amphipols. Protein particles on the EM grid showed round shape and size consistent with the design model (scale bar at the bottom left, 100 nm). Inset, close-up view of representative particles; each side of the particle frames represent 12.8 nm. **d**, Disrupting mutation in the TMHC6 pore entrance reduces the current. The E44F single mutant reduced the K^+ current to half that of TMHC6. TMHC2, a previously designed transmembrane protein without a pore, does not conduct ions across the membrane. Three cells were measured for each protein; data are mean ± s.e.m. **e**, The covalent modification of TMHC6(E44C) by MTSES. Mass spectrometry analysis that there is a 140 Da increase in molecular mass for the mutant after MTSES treatment, in agreement with the predicted value. **f**, Expression of TMHC6 and mutants in insect cells for the whole-cell patch-clamp experiments. The same amount of cells were loaded into the gel and the expression levels for two variants were examined by western blot. The E44F mutant had a similar, if not higher, expression level to TMHC6. The E44C mutant was expressed at a slightly lower level compared to TMHC6. These experiments were repeated three times with similar results.

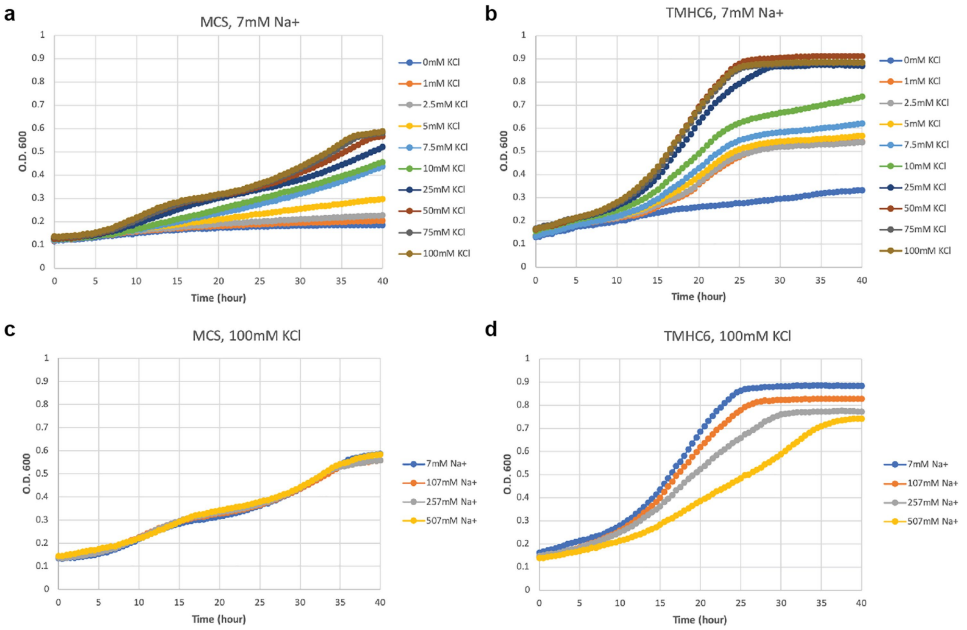

Extended Data Fig. 4 | The expression of TMHC6 complements a yeast strain defective in K^+ uptake. a, SGY1528 with an empty vector MCS grew slowly when K^+ concentration was lower than 5 mM. The observed growth rate showed dependency on extracellular K^+ concentration. **b**, SGY1528 supplemented with the TMHC6 gene rescued the yeast growth at lower extracellular K^+ concentrations (1 mM–5 mM) and showed increased growth rates at higher extracellular K^+ concentrations (7.5 mM–100 mM). **c**, **d**, With increasing concentrations of extracellular Na^+, TMHC6 yeast showed decreased growth rate (**d**) in comparison with the insensitive growth rates of MCS yeast (**c**). These results suggest that TMHC6 conducts K^+ and complements the defective K^+ uptake in strain SGY1528; this rescuing effect is sensitive to extracellular Na^+ concentrations indicating an increased Na^+ permeability. Detailed methods are described in the Supplementary Information. The minimal medium and the seeding process are carefully designed to not contain or bring in potassium. The background K^+ concentration should be low, which is suggested by the sharp difference between curves for 0 and 1 mM K^+ in the case of TMHC6.

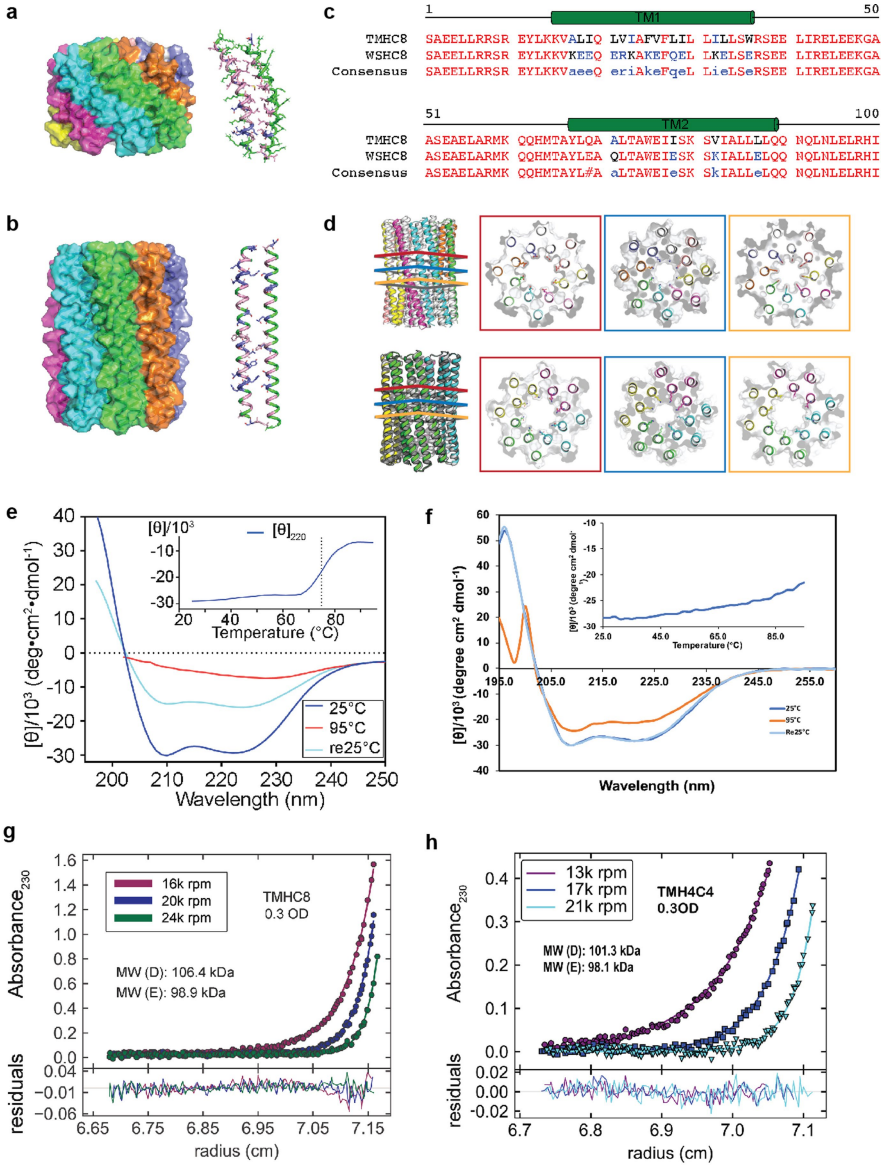

Extended Data Fig. 5 | Design and additional characterizations of the designed 16-helix pores. a, **b**, Design models from the first and second rounds of water-soluble designs. The monomers of the first round designs (**a**, 70 amino acids) are considerably smaller than those of the second round (**b**, 100 amino acids). **c**, Sequence alignment of TMHC8 with WSHC8. **d**, Pore-lining residues in WSHC8 and TMH4C4. The crystal and cryo-EM structures are in colours. The design models are in grey. Top row, the lumen of WSHC8 pore is freely water-accessible, so the residues inside the pore are all polar. Shown in the figure are three representative layers of the pore-lining residues in the crystal structure, Glu69 ring (red), Lys80 ring (blue), and Glu87 (orange). The missing heavy atoms of these flexible residues are built using Rosetta with backbone constraints. Bottom row, three pore-lining layers in the cryo-EM structure of TMH4C4 corresponding to the three layers in the top row. Glu69 and Glu87 are replaced with glutamine and leucine, respectively. **e**, **f**, Circular dichroism spectra and thermal stability of 16-helix transmembrane pores. An unfolding transition is observed at around 75 °C for TMHC8 (**e**). TMH4C4 (**f**) is thermally stable up until 95 °C. **g**, **h**, Representative AUC sedimentation-equilibrium curves of 16-helix transmembrane nanopores. By fitting the data globally as a single ideal species in solution, TMHC8 is shown to form complexes with a molecular mass of 98.9 kDa, which is in between the masses of a heptamer and an octamer. The molecular mass of TMH4C4 is determined to be 98.1 kDa, very close to that of a tetramer. 'MW (D)' refers to the molecular mass of the oligomer design and 'MW (E)' refers to the molecular mass determined in the experiment.

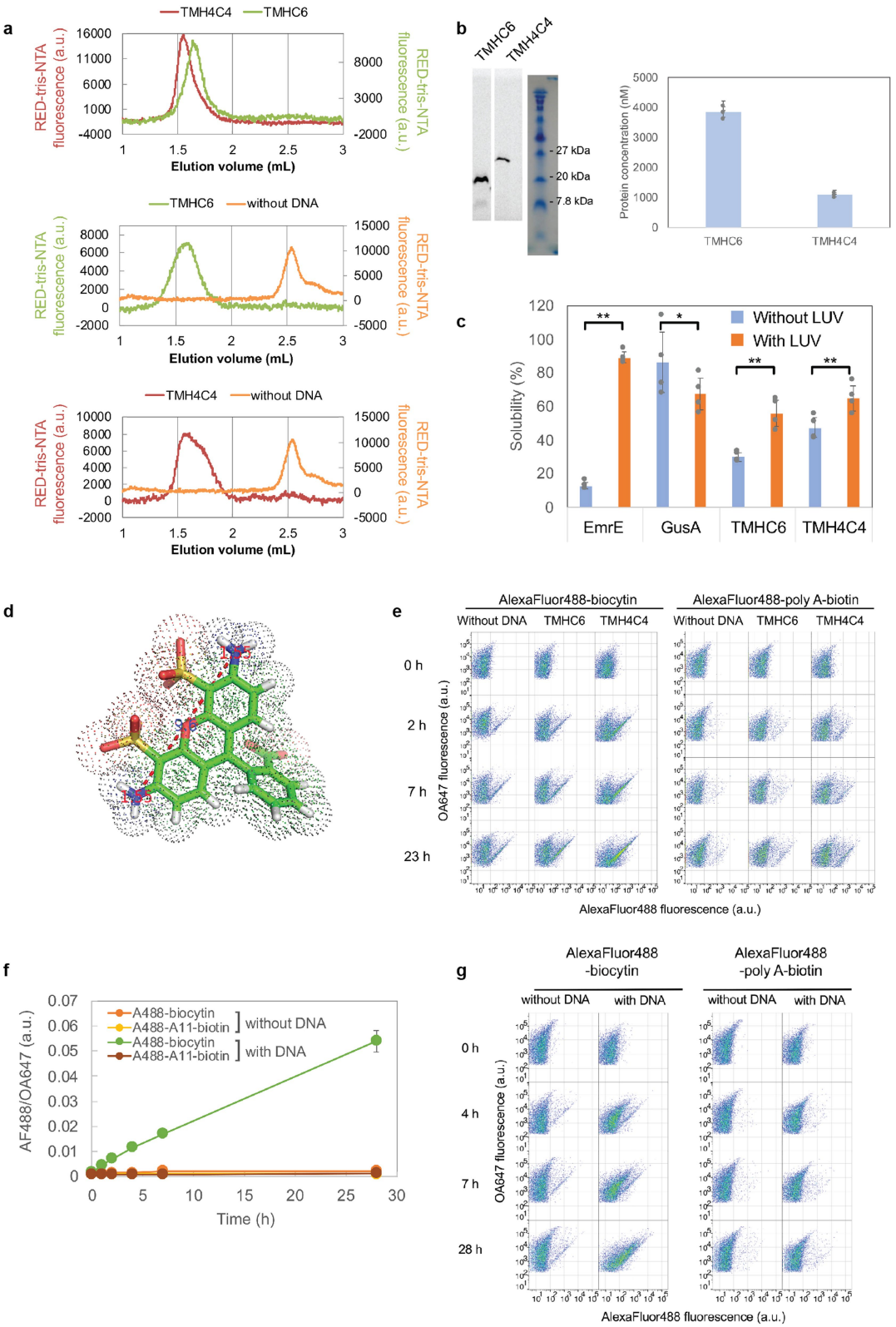

Extended Data Fig. 6 | See next page for caption.

Extended Data Fig. 6 | In vitro protein synthesis and characterizations of TMHC6 and TMH4C4. a, SEC analyses of TMHC6 and TMH4C4 purified from *E. coli* (top) and synthesized in vitro (middle and bottom). **b**, The in vitro synthesized products were analysed by SDS–PAGE and autoradiography. The means of three independent experiments are shown. The error bars indicate s.e.m. **c**, EmrE, one of the *E. coli*-derived membrane proteins, showed strong interaction with LUV, whereas GusA, a soluble enzyme, did not. For TMHC6 and TMH4C4, the fraction interacting with LUV was found to be 25.9% and 17.6%, respectively, among synthesized, indicating that the fraction associated with the membrane is similar between them. The mean of four independent experiments are shown. The error bars indicate s.e.m. Student's paired *t*-test with a two-sided distribution was used to calculate the *P* values (*$P < 0.05$, **$P < 0.01$; from left to right $P = 1.65 \times 10^{-6}$, 0.0357, 0.0040, 0.0024). **d**, The narrowest dimension of the head group of Alexa Fluor 488–biocytin is approximately 12 Å. The van der Waals radius of nitrogen atoms is 1.55 Å. **e**, Representative original data for Fig. 3f. Data of approximately 15,000 to 20,000 particles are shown. Similar results were obtained with 7 independent experiments. **f**, Flow cytometry data of the liposomes with pores made of α-haemolysin (AH). Time courses of the median values of the histogram of AF488/OA647 fluorescence, which represents the concentration of the Alexa Fluor 488 inside the liposome, are shown. The means of three independent experiments are plotted with the error bars indicating the s.e.m. **g**, Representative original data of **f**. Similar results were obtained with 3 independent experiments.

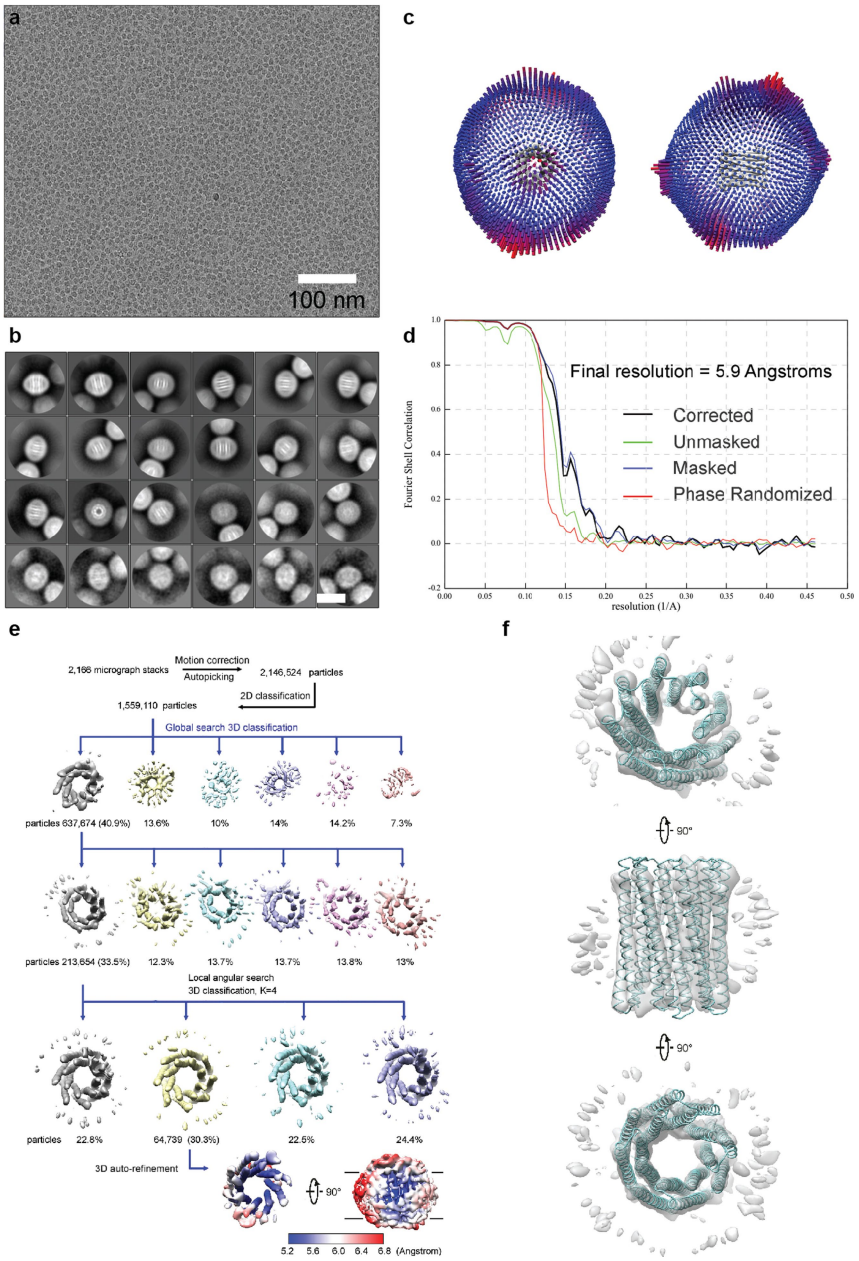

Extended Data Fig. 7 | Cryo-EM resolution estimation and data processing. **a**, Exemplary cryo-EM micrograph of purified TMH4C4 after drift correction and dose-weighting. All the micrographs showed similar results. **b**, Class averages after the final round of 2D classification sorted in descending order by the number of particles in each class. The white scale bar in the bottom right panel indicates 10 nm. **c**, Angular distribution plot for the final reconstruction from two different views. **d**, The gold-standard Fourier shell correlation (FSC) curves for the 3D reconstruction. Deriving map resolution from FSC = 0.143 is indicated. **e**, Processing of 2,166 EM micrographs resulted in a total number of 2,146,524 TMH4C4 particles. After a 2D sub-classification, 3D classifications and refinement, a final data set containing 64,739 particles was used for 3D auto-refinement within RELION 3.0. Local resolution of TMH4C4 was determined within RELION 3.0. Coloured full views (lower lane) from two different orientations illustrate the resolution of different regions in the protein. The low resolution 'belt' in the right panel indicates the density for detergents. **f**, EM density from 213,654 particles. An EM map (grey) from the second round of 3D classification from 213,654 particles (**e**) is shown in three perpendicular views. Superposition of the cryo-EM structure of TMH4C4 (cyan) to the map shows a good fit.

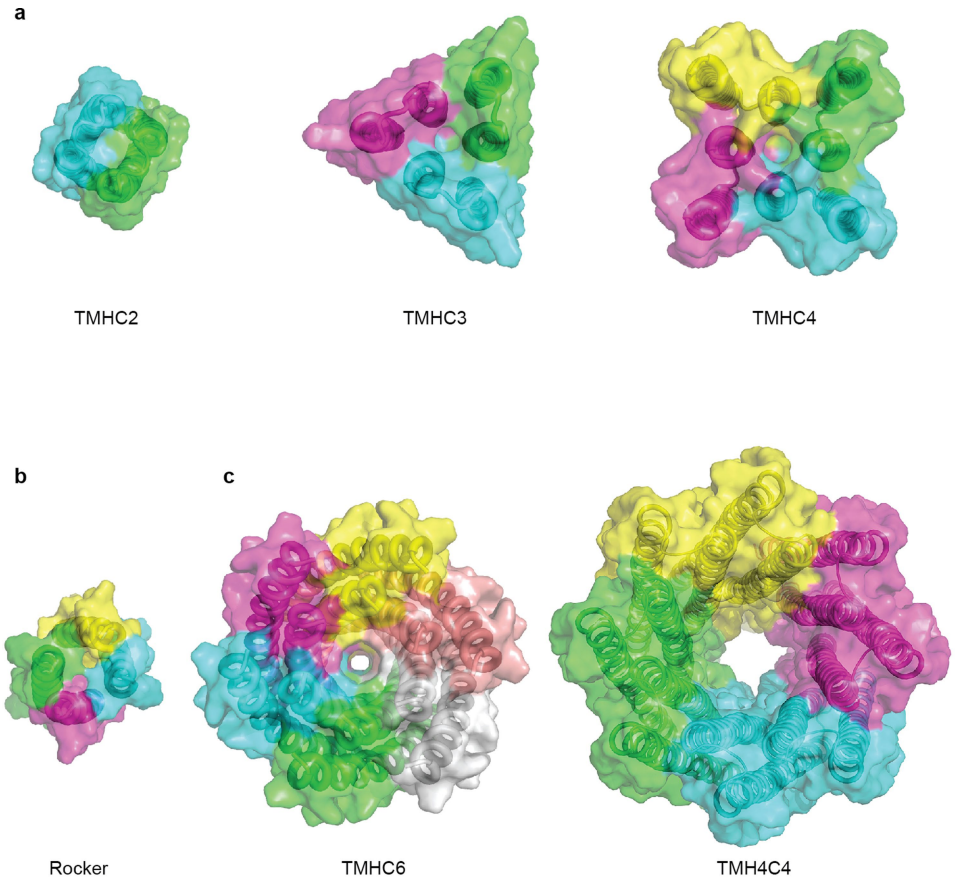

Extended Data Fig. 8 | Advances in membrane protein design, from compact helical bundles to transmembrane pores. a, **b**, Surface view of previously reported de novo designed transmembrane proteins[7,8]. **c**, Surface view of designer transmembrane pores described in this study. Central pores with different sizes are visible.

Extended Data Table 1 | Crystallographic statistics for WSHC6 and WSHC8

	WSHC6	WSHC6	WSHC8
Data collection			
Space group	$P2_122_1$	P1	$P2_12_12$
Cell dimensions			
a, *b*, *c* (Å)	45.72, 54.13, 79.17	45.88, 54.33, 79.33	59.44, 103.68, 72.98
a, b, g (°)	90, 90, 90	89.80, 90.08, 89.77	90, 90, 90
Resolution (Å)	45.7-2.35	54.2 – 2.6	34.4 - 2.4 (2.49 - 2.4)
R_{sym} or R_{merge}	0.114 (0.561)	0.145 (0.648)	0.192 (1.698)
I / s*I*	10.7 (1.5), 8.6 (0.7), 9.6 (2.5)[#]	5.0 (1.4), 4.9 (1.0), 7.0 (2.6)[#]	8.3 (1.4)
Completeness (%)	95.3 (95.6)	98.7 (98.7)	99.6 (99.4)
Redundancy	2.8 (2.9)	3.0 (3.0)	7.0 (7.2)
Refinement			
Resolution (Å)	40.0 - 2.4	20 - 2.6	34.4 - 2.4
No. reflections	14091	44867	18183
R_{work} / R_{free}	0.254/0.288	0.279/0.287	0.261/0.298
No. atoms	1641	7215	2931
Protein	1608	6674	2914
Ligand/ion			
Water	33	541	17
B-factors	67.9	48.0	59.4
Protein	68.3	46.5	59.5
Ligand/ion		41.6	
Water	49.0	57.0	43.8
R.m.s. deviations			
Bond lengths (Å)	0.004	0.095	0.002
Bond angles (°)	0.86	2.57	0.37

*Data for WSHC6 and WSHC8 structures were collected from a single crystal. Values in parentheses are for the highest-resolution shell.
[#]I/σ(I) (along a*, b* and c* axes).

Extended Data Table 2 | Cryo-EM image processing statistics for TMH4C4

	TMH4C4 (EMD-30126) (PDB-6M6Z)
Data collection and processing	
EM equipment	Titan Krios (Thermo Fisher Scientific)
Magnification	81,000
Voltage (kV)	300 kV
Detector	Gatan K3 Summit
Energy Filter	Gatan GIF Quantum, 20 eV slit
Electron exposure (e–/Å^2)	50
Defocus range (μm)	-1.2 ~ -2.2
Pixel size (Å)	1.087
Initial particle images (no.)	2,146,524
Final particle images (no.)	64,739
Symmetry imposed	C1
Map resolution (Å)	5.9
FSC threshold	0.143
Map resolution range (Å)	5.2 - 7.2
Refinement	
Initial model used (PDB code)	n/a (*de novo*)
Model resolution (Å)	7.7
FSC threshold	0.5
Map sharpening *B* factor (Å^2)	-292
Model composition	
Non-hydrogen atoms	6600
Protein residues	804
Ligands	n/a
R.m.s. deviations	
Bond lengths (Å)	0.016
Bond angles (°)	1.3
B factors (Å^2)	
Protein	169.4
Ligand	n/a
Validation	
MolProbity score	0.52
Clashscore	0.05
Poor rotamers (%)	0
Ramachandran plot	
Favored (%)	99.63
Allowed (%)	100
Disallowed (%)	0

nature research

Corresponding author(s): David Baker

Last updated by author(s): Apr 23, 2020

Reporting Summary

Nature Research wishes to improve the reproducibility of the work that we publish. This form provides structure for consistency and transparency in reporting. For further information on Nature Research policies, see Authors & Referees and the Editorial Policy Checklist.

Statistics

For all statistical analyses, confirm that the following items are present in the figure legend, table legend, main text, or Methods section.

n/a	Confirmed	
☐	☒	The exact sample size (*n*) for each experimental group/condition, given as a discrete number and unit of measurement
☐	☒	A statement on whether measurements were taken from distinct samples or whether the same sample was measured repeatedly
☐	☒	The statistical test(s) used AND whether they are one- or two-sided *Only common tests should be described solely by name; describe more complex techniques in the Methods section.*
☒	☐	A description of all covariates tested
☒	☐	A description of any assumptions or corrections, such as tests of normality and adjustment for multiple comparisons
☐	☒	A full description of the statistical parameters including central tendency (e.g. means) or other basic estimates (e.g. regression coefficient) AND variation (e.g. standard deviation) or associated estimates of uncertainty (e.g. confidence intervals)
☒	☐	For null hypothesis testing, the test statistic (e.g. *F*, *t*, *r*) with confidence intervals, effect sizes, degrees of freedom and *P* value noted *Give P values as exact values whenever suitable.*
☒	☐	For Bayesian analysis, information on the choice of priors and Markov chain Monte Carlo settings
☒	☐	For hierarchical and complex designs, identification of the appropriate level for tests and full reporting of outcomes
☒	☐	Estimates of effect sizes (e.g. Cohen's *d*, Pearson's *r*), indicating how they were calculated

Our web collection on statistics for biologists contains articles on many of the points above.

Software and code

Policy information about availability of computer code

Data collection	Rosetta software suite 3 was used for protein design calculations. AVIV Data Collection software v3.45 was used for CD. ProteomeLab XL-I for AUC. AutoEMation for cryoEM. Igor Pro 6.37 software for patch-clamp experiments. BD FACSuite v1.0.5.3841 for FACS.
Data analysis	Sedfit 15.1b, Sednterp 20120828 beta and Sedphat 14.0 were used for AUC data analysis. CRYSOL and SASPLOT in ATSAS 2.7.2 for SAXS data analysis. XDS version Jan 26, 2018, Phaser, version 2.8.2., Phenix.refine version dev_3112, Phenix version 1.11.1-2575, and iMosflm from CCP4 V7 for X-ray data analysis. RELION 3.0.6 and Chimera 1.13.1 for cryoEM data processing and refinement. FlowJo v10.6.2 for FACS analysis. Protein structures and models were visualized using PyMOL 1.7.6.5 HOLE 2.0 for calculating designed pore radius. TMHMM server 2.0 for predicting membrane compatibility of designed proteins.

For manuscripts utilizing custom algorithms or software that are central to the research but not yet described in published literature, software must be made available to editors/reviewers. We strongly encourage code deposition in a community repository (e.g. GitHub). See the Nature Research guidelines for submitting code & software for further information.

Data

Policy information about availability of data

All manuscripts must include a data availability statement. This statement should provide the following information, where applicable:

- Accession codes, unique identifiers, or web links for publicly available datasets
- A list of figures that have associated raw data
- A description of any restrictions on data availability

Coordinates and structure files have been deposited to the Protein Data Bank with accession codes 6TJ1 and 6TMS (WSHC6) and 6O35 (WSHC8). EM structure of TMH4C4 and the associated atomic model have been deposited in the Electron Microscopy Data Bank and Protein Data Bank with the following accession codes: EMD-30126 and PDB 6M6Z. AUC, CD, patch-clamp, and FACS experiments in the main figures have associated raw data.

Field-specific reporting

Please select the one below that is the best fit for your research. If you are not sure, read the appropriate sections before making your selection.

☒ Life sciences ☐ Behavioural & social sciences ☐ Ecological, evolutionary & environmental sciences

For a reference copy of the document with all sections, see nature.com/documents/nr-reporting-summary-flat.pdf

Life sciences study design

All studies must disclose on these points even when the disclosure is negative.

Sample size	Water-soluble and transmembrane pores were designed by the Rosetta software suite and designs passing computational selection criteria were experimentally tested. Based on the previously reported success rate of designing proteins with similar topologies using Rosetta, we estimated the number of designs we should test in order to be successful. The number of designs tested was increased after the first round of design failed to create an octamer.
Data exclusions	No data were excluded from the study.
Replication	Oligomerization states of designed proteins were verified by more than one biophysical methods: MALS, AUC and SAXS. Standard measures were taken to ensure crystallographic and EM analysis were done correctly. Electrophysiological studies and liposome permeability assays were repeated at least once to make sure findings were reproducible. All attempts at replication were successful.
Randomization	No randomized sample allocation in this work. Because of the complexity of the designs, it is unlikely that the amino acids sequences reported in this paper are due to chance rather than design calculation. Negative and positive controls were well defined and validated.
Blinding	Not relevant to the study since the experiments were well-defined by the computational design.

Reporting for specific materials, systems and methods

We require information from authors about some types of materials, experimental systems and methods used in many studies. Here, indicate whether each material, system or method listed is relevant to your study. If you are not sure if a list item applies to your research, read the appropriate section before selecting a response.

Materials & experimental systems

n/a	Involved in the study
☒	☐ Antibodies
☐	☒ Eukaryotic cell lines
☒	☐ Palaeontology
☒	☐ Animals and other organisms
☒	☐ Human research participants
☒	☐ Clinical data

Methods

n/a	Involved in the study
☒	☐ ChIP-seq
☐	☒ Flow cytometry
☒	☐ MRI-based neuroimaging

Eukaryotic cell lines

Policy information about cell lines

Cell line source(s)	Trichoplusia ni insect cells (Hi5, Thermo Fisher); Yeast strain SGY1528 shared by Lily Jan lab at UCSF.
Authentication	The cell lines were not authenticated.
Mycoplasma contamination	The cell lines were not tested for Mycoplasma contamination.
Commonly misidentified lines (See ICLAC register)	No misidentified cell lines were used for this study.

Flow Cytometry

Plots

Confirm that:

☒ The axis labels state the marker and fluorochrome used (e.g. CD4-FITC).

☒ The axis scales are clearly visible. Include numbers along axes only for bottom left plot of group (a 'group' is an analysis of identical markers).

☒ All plots are contour plots with outliers or pseudocolor plots.

☒ A numerical value for number of cells or percentage (with statistics) is provided.

Methodology

Sample preparation	The analyzed samples are liposomes prepared by water-in-oil emulsion transfer method (Nishimura et al., Langmuir, 2012)
Instrument	FACSVerse (BD, Franklin Lakes, NJ)
Software	FlowJo (BD, Franklin Lakes, NJ)
Cell population abundance	30,000 liposomes were used for analysis.
Gating strategy	Liposomes with AlexaFluor647 fluorescence>10^2 were used for analysis.

☒ Tick this box to confirm that a figure exemplifying the gating strategy is provided in the Supplementary Information.